In situ transmission electron microscopy studies of electric-field-induced phenomena in ferroelectrics

Xiaoli Tan[a] and Hui He
Department of Materials Science and Engineering, Iowa State University, Ames, Iowa 50011
Jian-Ku Shang
Department of Materials Science and Engineering, University of Illinois at Urbana-Champaign, Urbana, Illinois 61801

(Received 6 January 2005; accepted 25 March 2005)

High electric fields were delivered to specimens during imaging in the transmission electron microscopy (TEM) chamber to reveal details of electric field-induced phenomena in ferroelectric oxides. These include the polarization switching in nanometer-sized ferroelectric domains and the grain boundary cavitation in a commercial lead zirconate titanate (PZT) polycrystalline ceramic, the domain wall fracture in a $Pb(Mg_{1/3}Nb_{2/3})O_3$–$PbTiO_3$ single crystal, and the transformation of incommensurate modulations in $Pb_{0.99}Nb_{0.02}[(Zr_{1-x}Sn_x)_{1-y}Ti_y]_{0.98}O_3$ (PZST100*x*/100*y*/2) polycrystalline ceramics. In the PZT ceramic, a cavitation process was uncovered for the electric field-induced intergranular fracture. In the ferroelectric single crystal, a preexisting crack was observed to deflect and to follow a 90° domain wall, indicating the presence of severe incompatible piezoelectric strains at the domain wall. In the antiferroelectric PZST ceramics, the electric field-induced antiferroelectric-to-ferroelectric phase transformation was accompanied with the disappearance of incommensurate modulations.

I. INTRODUCTION

Many materials respond to external electric field/current by changing their microstructures. Transmission electron microscopy (TEM) allows one to examine the microstructure in inorganic materials with spatial and chemical resolutions on the atomic level, so attempts have been made to apply electrical signals to TEM specimens while imaging in the hope of revealing the dynamic processes at the nanometer scale. Although such electrical in situ TEM techniques were demonstrated in as early as 1960s when Blech and Meieran were passing a direct current (dc) electrical current through an Al thin film to observe the electromigration process,[1] there are only a handful of publications based on this technique at this time. Most of them are studies on the electromigration in interconnecting lines[1–5] and the domain switching in ferroelectrics.[6–11] Recently, the application of this technique has been expanded to studies of other phenomena, such as the failure mechanism of solid electrolytes,[12] the breakdown of grain boundary conducting barrier,[13] and the mechanical fatigue of metallic thin films.[14] The present article focuses on the electric field-induced phenomena in perovskite ferroelectrics. It summarizes our previous contributions to this field[15–19] and presents our new findings on the antiferroelectric-to-ferroelectric phase transformation in ceramics with incommensurate modulations.

Ferroelectric ceramics have found wide applications in capacitors, transducers, actuators, energy storage devices, and random-access memory due to their unique dielectric, piezoelectric, and ferroelectric properties. In most cases, these materials are subjected to strong electric fields. The primary response of the microstructure in ferroelectrics to external electric fields is the polarization switching through domain wall motion.[20] When the applied field is sufficiently high and yet lower than the dielectric-breakdown strength, phase transformations can be triggered.[21–25] Among these electric-field-induced phase transformations, the antiferroelectric-to-ferroelectric one forms the physics foundation for applications of antiferroelectrics in the energy storage and large displacement control devices.[21,22] However, when driven hard with bipolar electric fields for extended cycles, ferroelectric materials may lose their physical integrity due to grain boundary cracking.[26–29] Our studies with the unique electric field in situ TEM technique, for

[a]Address all correspondence to this author.
e-mail: xtan@iastate.edu
DOI: 10.1557/JMR.2005.0213

the first time, directly visualized the dynamic process of the polarization switching of nanometer-sized domains and the cavitation of grain boundaries in ferroelectric ceramics, the fracture of domain walls in ferroelectric single crystals, and the evolution of incommensurate modulations in antiferroelectric ceramics.

Previous studies on ferroelectrics with electric field in situ TEM technique by other researchers are limited to the polarization switching of ferroelectric domains.[6–11] The electric field was applied to the specimen by two parallel TEM copper grids through a configuration shown in Fig. 1. The nominal electric field is parallel to the electron beam, and therefore, negligible disturbance to the TEM imaging can be achieved. However, a major drawback of this configuration is that the actual electric field in the thin area of the specimen is far less than the nominal field. Furthermore, the magnitude of the actual field is hard to estimate due to the presence of the vacuum gaps between the copper grid electrodes and the specimen.

We modified the electrode configuration by depositing gold films directly on the TEM specimen surface for better quantifying the actual field (Fig. 2). In this configuration, the presence of the central hole disturbs the electric field within the specimen. According to McMeeking's[30] and Suo's[31] analytical solutions for the electric field disturbed by a perpendicular insulating flaw, the direction of the actual field at the flaw tip remains unchanged, but the magnitude is intensified. The intensification ratio depends on the geometry of the flaw and the dielectric permittivity. When the flaw is a circular hole penetrating through the thickness and the dielectric permittivity of the ferroelectric material is much greater than that of the material filled in the flaw, the intensification ratio is 2. The specimen geometry used in our study is shown in Fig. 2(a). We may consider the central perforation as the insulating flaw, and in most cases the perforation takes a circular shape. When the specimen is loaded into the TEM chamber, the flaw is filled with a vacuum with a relative permittivity of 1. The ferroelectric ceramic materials studied here have relative dielectric permittivity greater than 300 at room temperature.[15–19] As a rough approximation, the intensification ratio can be taken as 2 at the tip of the central perforation if the effect of the thickness variation due to the mechanical dimpling is ignored. In Fig. 2(a), the two tips of the central perforation are exaggerated and highlighted by the two dark areas. We selected circularly perforated TEM specimens without cracks for all in situ studies and carried our observations at these two sites. In this way, the direction of the actual electric field can be determined by finding out the direction of the nominal field, and the magnitude of the actual field can be estimated by doubling the nominal electric field. All the field levels stated for the in situ TEM experiment in this article refer to this actual field.

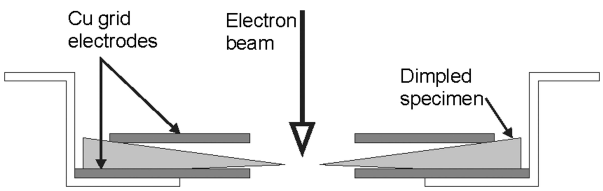

FIG. 1. The configuration used by previous researchers for studying electric field-induced domain switching in ferroelectric ceramics.

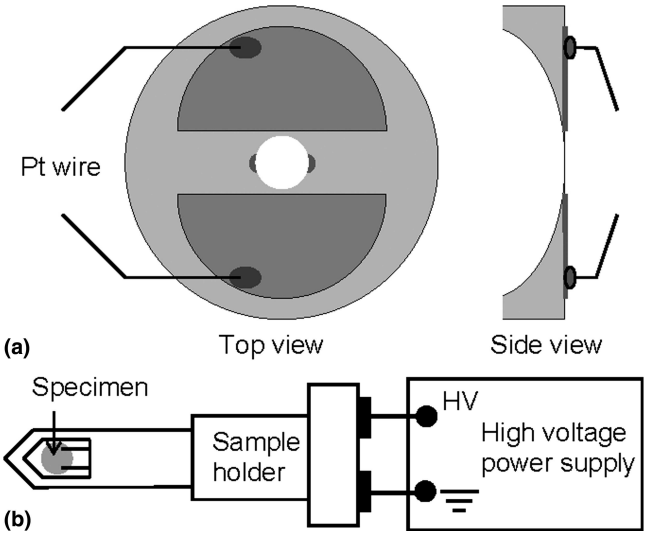

FIG. 2. Electric field in situ TEM experimental setup used in this study. (a) The specimen geometry shows the two half-circle shaped gold electrodes and the central perforation. The two small dark areas at the edge of the perforation exaggerate and highlight the two tips of the circular flaw. In this study, all the in situ TEM observations were made at electron transparent areas at these two sites. (b) The test system was composed of a special TEM holder and a high voltage power supply.

II. EXPERIMENTAL

TEM specimens were prepared via conventional procedures including polishing, dimpling, and ion milling. Half-circle shaped gold electrodes were coated on the flat surfaces of the 3-mm disks, as shown in Fig. 2(a). A special mask was utilized to form the central gap. The electroded specimens were examined with optical microscopy, and crack-free specimens were loaded to a special TEM holder with two electrical feedthroughs. TEM specimens were fixed on the bottom of the sample cup using insulating varnish. Connections were made from the electrical leads on the holder tip to the gold electrodes on the specimen through thin platinum wires. A high-voltage source was connected to the outside terminals of the sample holder, as shown in Fig. 2(b). Both static and cyclic electric fields with amplitudes up to 60 kV/cm were applied to the specimens during in situ studies. A frequency of 30 Hz was used for the applied

cyclic electric fields. Since the applied field was perpendicular to the optic axis of the TEM, it caused electron beam deflection, which was compensated for by adjusting beam deflection on the microscopy. TEM experiments were carried out with a single-tilt specimen holder on a Phillips CM-12 microscope (Eindhoven, Netherlands) operating at 120 kV for the work shown in Secs. III. A–C and with a double-tilt holder on a Phillips CM-30 microscope (Eindhoven, Netherlands) operating at 300 kV for the work shown in the Sec. III. D.

III. RESULTS AND DISCUSSION

A. Domain polarization switching

The electric field in situ TEM technique with the modified electrode configuration was first tested with a commercial lead zirconate titanate (PZT) ceramic (PZT EC65, EDO Corporation, Salt Lake City, UT).[15] The ceramic has an average grain size of 8 μm and a mixed nanometer-sized and micrometer-sized domain structure. It contained 4% porosity with most pores smaller than 30 μm in size. At room temperature, the ceramic has a tetragonal crystal structure and a ferroelectric coercive field of 8 kV/cm.

The regular lamellar 90° ferroelectric domains in this tetragonal ceramic were disrupted by proprietary chemical dopants. These disrupted polar domains appeared as nanometer-sized dark patches in the bright-field TEM images.[11] Since the PZT EC65 ceramic shows normal ferroelectric behavior and displays a tetragonal perovskite symmetry, these disrupted domains are believed to be 90° ferroelectric domains. The diffraction contrast mechanism in TEM is hence originated from the difference in polar axis across the domain wall and from the strain field associated with the domain wall. The evolution of the morphology of the nanometer-sized domains under external electric field for the very first 1 1/4 cycles was recorded and is shown in Fig. 3. A diagram of the field strength variation E with time t is inserted in the figure for the sake of clarification. Static fields were stepwise increased and images were taken at field levels of 0, +40, +80, 0, −40, −80, and +80 kV/cm, respectively. The bright-field images were recorded from the interior of a single grain with its $\langle 1\bar{1}1\rangle$ direction parallel to the electron beam under multi-beam condition. The white arrow in Fig. 3(a) indicates the in-plane $\langle 110\rangle$ crystallographic direction and the white arrows in Figs. 3(b)–3(f) denote the directions of the applied electric fields.

Initially at the thermally de-poled state, the nanometer-sized domains showed some extent texture [Fig. 3(a)]. When the electric field increased to +40 kV/cm, these short-range features broke up and reorganized [Fig. 3(b)]. At +80 kV/cm, these irregular-shaped domains were forced to align along the {110} plane. A nearly contrast-free zone between these aligned domains appeared, as shown in Fig. 3(c). The aligned domains remained during the second quarter of the electrical cycle when the field was decreased to zero [see Fig. 3(d)]. Upon reversing the electric field to −80 kV/cm, these aligned domains were disrupted [Fig. 3(e)]. Returning

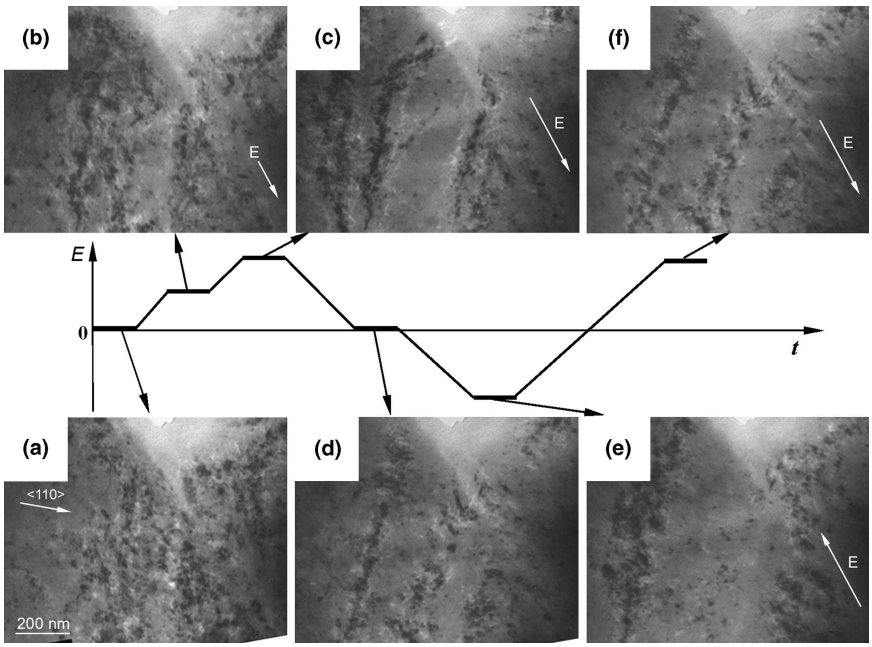

FIG. 3. Bright field TEM images of the morphology of nanometer-sized ferroelectric domains in the PZT EC65 ceramic at different field levels: **B**//$\langle 1\bar{1}1\rangle$; multi-beam condition: (a) initial morphology, (b) +40 kV/cm, (c) +80 kV/cm, (d) 0 kV/cm, (e) −80 kV/cm, and (f) +80 kV/cm. The in-plane $\langle 110\rangle$ direction is shown in (a). The white arrows in (b), (c), (e), (f) indicate the field direction.

the external field to +80 kV/cm partially recovered the domain structure at the previous application of the +80 kV/cm level [Fig. 3(f)].

For the tetragonal PZT-EC65 ceramic examined in this study, proprietary dopants were added to disrupt the regular micrometer-sized domains to optimize the piezoelectric properties. After thermal annealing, the ceramic lost piezoelectricity but remained ferroelectric. The electric field-induced domain switching involves both 180° and 90° polarization reorientation. The nearly contrast-free zone between aligned dark patches in Fig. 3(c) suggests that coalescence of those nanometer-sized domains took place under external fields.

B. Grain boundary cavitation

Extensive repeated domain polarization switching may cause failure of ferroelectric ceramics. One form of such failures is the grain boundary cracking in polycrystalline materials after they are subjected to extended cycling of bipolar electric fields.[26–29] It in interesting to notice that grain boundaries in these ceramics are not mechanically weak, and transgranular fracture features are typically observed under mechanical loadings.[26,27] Figure 4 shows the features revealed by scanning electron microscopy of a fracture surface generated by electrical and mechanical loadings in sequence in the PZT EC65 ceramic. An abrupt change in the fracture mode is evident when the crack growth driving force was switched from cyclic electric fields to mechanical bending. The electric field in situ TEM technique was applied to investigate the field-induced grain boundary fracture in this ferroelectric ceramic.[18]

Conventional TEM examination revealed that a thin amorphous layer exists along grain boundaries and pockets of amorphous phase accumulations were found at triple junctions of grain boundaries. Energy-dispersive spectrometry (EDS) analysis of the amorphous phase showed a composition with major components of Pb, Si, and Al. The abundance of Pb is believed to be a result of extra PbO added for compensating vaporization loss. Si and Al are among the impurities segregated to the grain boundaries. As uncovered by our in situ TEM study, it is the amorphous phase that caused the electric field-induced grain boundary cracking.

Figure 5 shows the development of microcracks from a pore in the PZT EC65 ceramic after repeated electrical cycling at a frequency of 30 Hz. The pore was located at

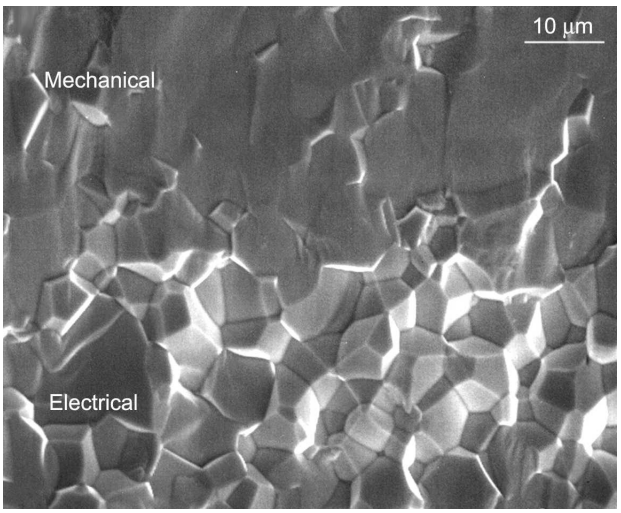

FIG. 4. Scanning electron microscopy image of the fracture surface of the PZT EC 65 piezoelectric ceramic. The ceramic fractured in an intergranular manner under electrical loadings while in a transgranular manner under mechanical loadings.

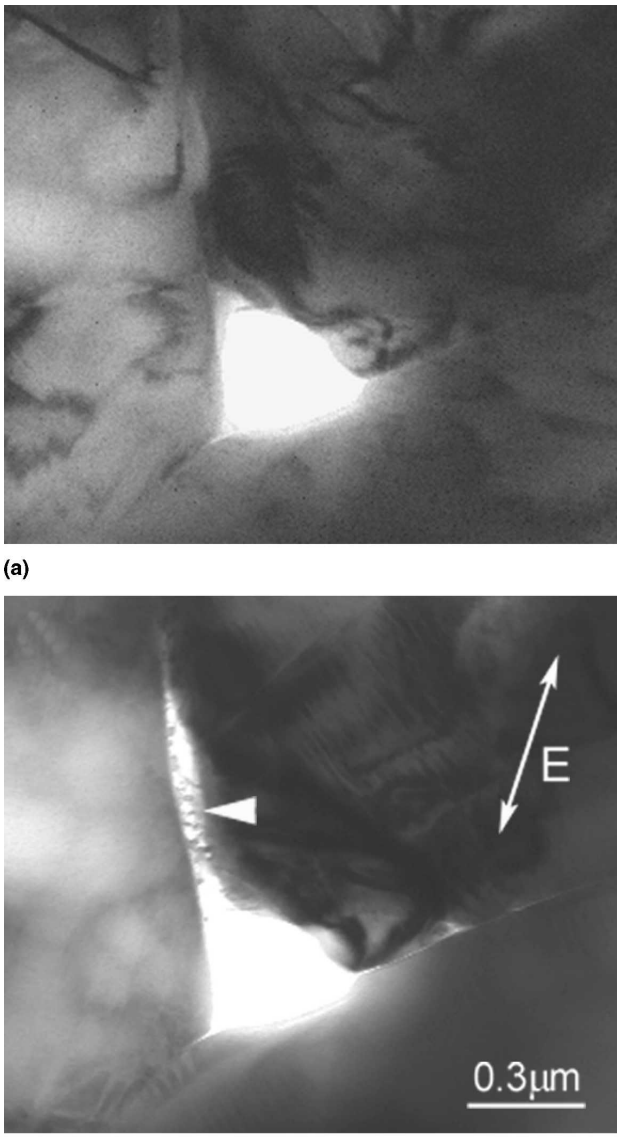

FIG. 5. Bright-field TEM images reveal that the electric field-induced fracture initiated from a pore at the triple junction of grain boundaries: (a) the initial morphology of the pore and (b) after 50,000 cycles of electric field of ±48 kV/cm. The bright arrow in (b) indicates the field direction. The microcrack was initiated through a cavitation process.

the triple junction of grain boundaries and was found about 5 μm from the central perforation. The defect was considered to be caused by sintering rather than ion milling during the TEM sample preparation. The initial morphology of the pore before application of the electric field is shown in Fig. 5(a) as an irregular bright triangle with corners pointing along three grain boundaries. When cyclic electric fields were applied along the direction of the arrow shown in Fig. 5(b), the three grain boundaries were inclined to the electric field. The morphology of the pore after cycling for 50,000 cycles at a field-amplitude of ±48 kV/cm is shown in Fig. 5(b). Comparison of Figs. 5(b) and 5(a) indicates that cracks developed from the corners of the pore and propagated along the grain boundaries. The field-induced cracking occurred along all three grain-boundaries, irrespective of their orientations, although one grain boundary experienced the most crack growth. The strong tendency of grain-boundary cracking is consistent with the intergranular nature of the field-induced crack growth observed in the same material of bulk form format.[27]

Close examination of the cracks revealed that cavities were formed along the grain boundary, as indicated by the bright triangle in Fig. 5(b). The cavities had diameters of 30–40 nm. They stayed isolated in part of the grain boundary but coalesced into a microcrack in another part of the boundary. The field-induced crack growth process appeared to consist of cavitation, microcrack formation, and coalescence. This was indeed the case, as shown by a series of images taken from a growing crack in Fig. 6. Initially, a grain boundary crack was induced from the edge of the perforation in the TEM specimen and was seen to extend to point A after 32,000 cycles at ±36 kV/cm. Ahead of the crack tip, local damage was found at point B, the triple junction of the grain boundaries [Fig. 6(a)]. As electric cycling continued, the crack tip advanced to point C [Fig. 6(b)]. During the same period, the damage at point B was extended into a microcrack, and the portion of the grain boundary between the crack tip (point C) and the microcrack (point B) was thinned, indicating that damage had occurred over that portion of the grain boundary. The form of the damage is shown in Fig. 7, magnified from the area marked by the square window in Fig. 6(b). The thinned section shown in Fig. 7 revealed again a nearly completely cracked area with cavities. Upon further electrical cycling, the portion of the grain boundary from point C to B was broken, and the crack tip moved ahead to beyond point B [Fig. 6(c)]. Such a cycle of cavity nucleation, growth, and coalescence was repeated as electrical cycling continued, resulting in stable crack growth along the grain boundary phase over many grains.

It is widely believed that the electric field-induced fracture in ferroelectric ceramics is caused by mismatch stresses resulting from incompatible piezoelectric

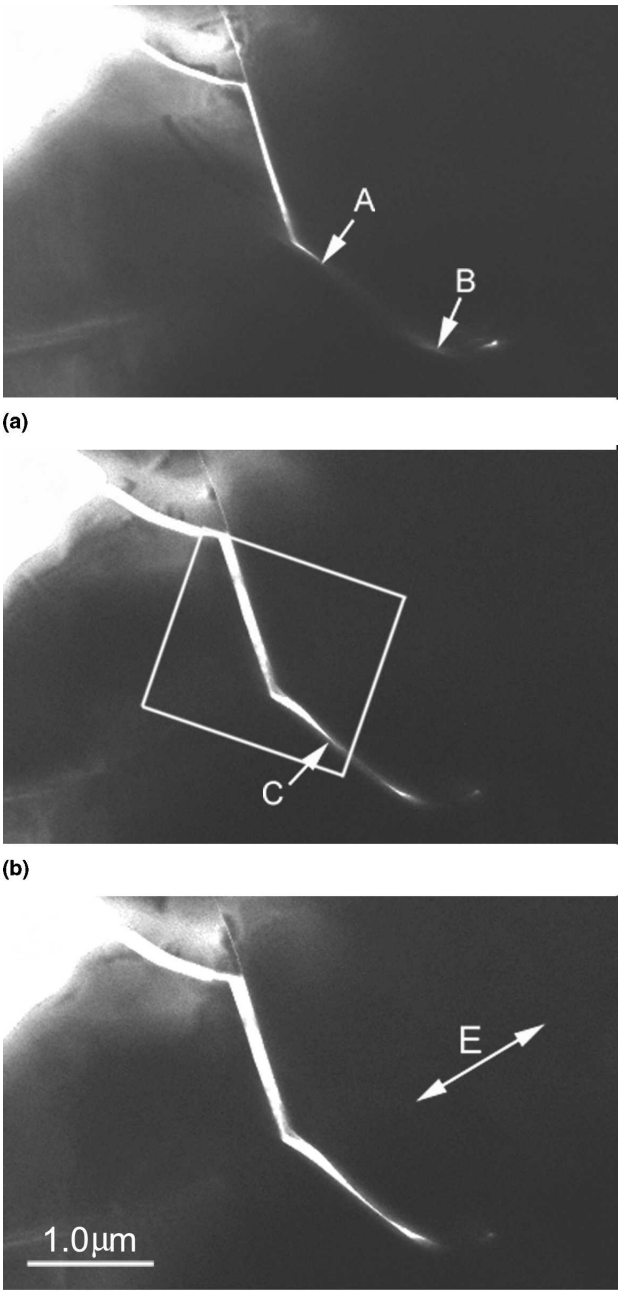

FIG. 6. Bright-field TEM images reveal the electric field-induced crack growth behavior: (a) after 32,000 cycles at ±36 kV/cm, (b) after 22,000 cycles at ±56 kV/cm, and (c) after 11,000 cycles at ±60 kV/cm. The direction of the electric field is indicated by the bright arrow in (c).

strain.[26–29] Under this assumption, the grain boundary cavitation process found in this in situ TEM study is unusual because it took place at room temperature where the grain boundary phase is expected to behave in a highly brittle manner under mechanical stresses. In fact, the cavitation of the glassy phase suggests that local melting of the grain boundary phase may have taken place during electrical cycling. We interpreted the field-induced grain boundary fracture process as follows. The

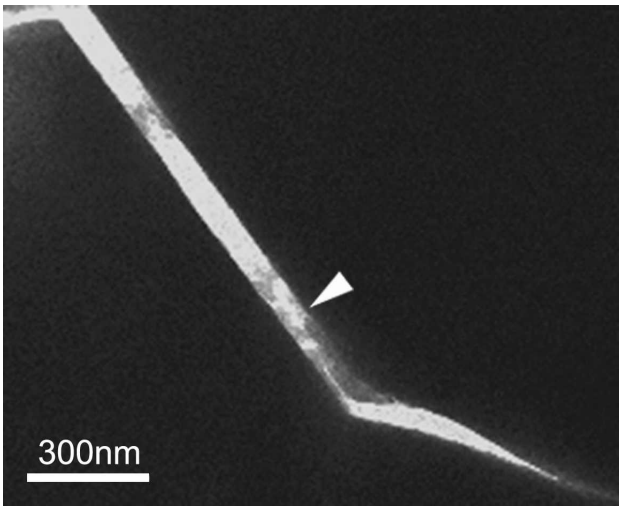

FIG. 7. Bright-field TEM image of the boxed area in Fig. 6(b). The bright triangle indicates the cavities in the glass ligament behind the crack tip.

amorphous phase was expected to have a much lower dielectric permittivity than the ferroelectric grain interior. The applied electric field was hence highly intensified at grain boundaries due to the field splitting effect. The intensified field led to local dielectric breakdown which in turn generated transient heat. Due to its low melting point, the amorphous phase melted for a transient period. It is suggested that the grain boundary cavities developed under incompatible piezoelectric stress during the transient heating. On the next pulse of the dielectric breakdown, additional cavities were added, and the remaining ligaments were further weakened, leading to coalescence of the cavities and the advance of the grain boundary crack.

Details of a semi-quantitative analysis of the observed field-induced fracture are provided in Ref. 18 where the local melting event was supported by estimation of several key parameters. In addition, the scenario of grain boundary phase melting pictured by the electric field in situ TEM study is in good agreement with previous studies in bulk dielectric ceramics. Beauchamp[32] noticed the correlation of dielectric-breakdown strength with grain size in MgO and observed, with optical microscopy, that dielectric breakdown always initiated at grain boundaries, most often at triple junction of grain boundaries. Ling and Chang[33] performed in situ optical microscopy study on the failure mechanism of $BaTiO_3$ multilayer capacitors. Indeed, they observed local melting and crack formation in the $BaTiO_3$ ceramic. Supporting evidence that it is more directly related to the current in situ TEM study was provided by Kanai and co-workers.[34] They evaluated the electric field induced failure in the relaxor ferroelectric ceramics of $(Pb_{0.875}Ba_{0.125})[(Mg_{1/3}Nb_{2/3})_{0.5}(Zn_{1/3}Nb_{2/3})_{0.3}Ti_{0.2}]O_3$ in the bulk form. In the Pb-rich ceramics, they observed continuous amorphous layers along grain boundaries and pockets of the amorphous phase at triple junctions of grain boundaries with TEM and the electric field-induced intergranular fracture at accelerated conditions (35 kV/cm, 85 °C, 95% relative humidity) with scanning electron microscopy. Most importantly, they found that the exposed grain boundaries on the fracture surface were full of cavities with diameters around 100 nm. Given consideration of the fact that dielectric breakdown occurred during their tests and the PbO-containing amorphous phase has a low melting point and a low glass transition temperature, these cavities may well be a result of local melting.

C. Domain wall fracture

Using piezoelectric single crystals avoids such grain boundary fracture, and in addition, much higher piezoelectric properties are expected. Unfortunately, growing PZT single crystals has proven to be very difficult. Recent studies of $Pb(Zn_{1/3}Nb_{2/3})O_3$–$PbTiO_3$ and $Pb(Mg_{1/3}Nb_{2/3})O_3$–$PbTiO_3$ have yielded large single crystals for compositions close to the rhombohedral/tetragonal morphotropic phase boundary in both systems. Indeed, these crystals exhibit ultrahigh piezoelectric properties.[23]

The in situ TEM technique was applied to a $0.65Pb(Mg_{1/3}Nb_{2/3})O_3$–$0.35PbTiO_3$ single crystal with tetragonal crystal structure to examine the response to external fields.[17] The TEM specimen was prepared from a {010} thin slice and the electrodes were so deposited that the nominal field was parallel to the ⟨001⟩ direction. As shown in Fig. 8(a), the crystal specimen in this area contained lamellar domains with widths of 0.1–0.5 μm. Convergent beam electron diffraction analysis indicated that these were 90° domains with in-plane polarization vectors. The domain walls were determined to be parallel to the {101} plane.

Also in the area shown in Fig. 8(a), a crack was generated during ion milling. This preexisting crack, about 3 μm long, was inclined to the domain walls. The dark arrow in Fig. 8(a) denotes the crack tip. First, static electric fields were applied to the specimen while the specimen was imaged in the TEM. The direction of the applied electric field was parallel to the ⟨001⟩ direction, as marked in Fig. 8(b). The field was increased gradually until crack growth was detected. Once the crack growth was observed, the electric field was turned off immediately. Figures 8(b) and 8(c) are photographs recorded from two successive applications of the static electric field. The arrows indicate the locations of the crack tip as it moved ahead. On the first application of the electric field, the crack growth was detected when the actual applied field reached 20 kV/cm. The resulting crack configuration is shown in Fig. 8(b), where the original crack had grown forward for a couple of domain spacings and then abruptly altered its direction to propagate along

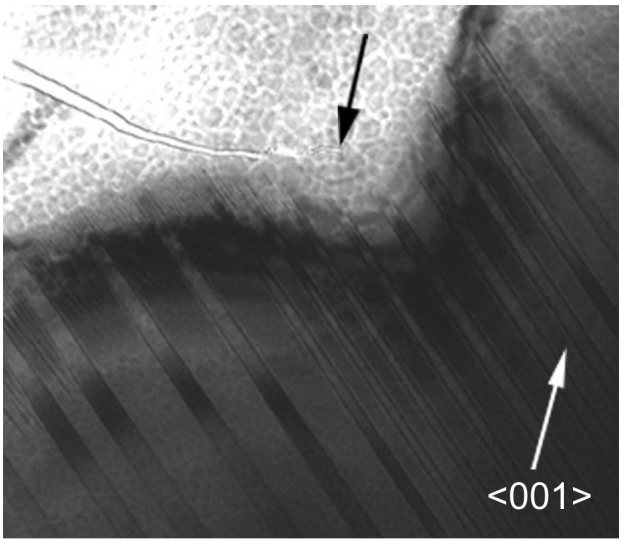

(a)

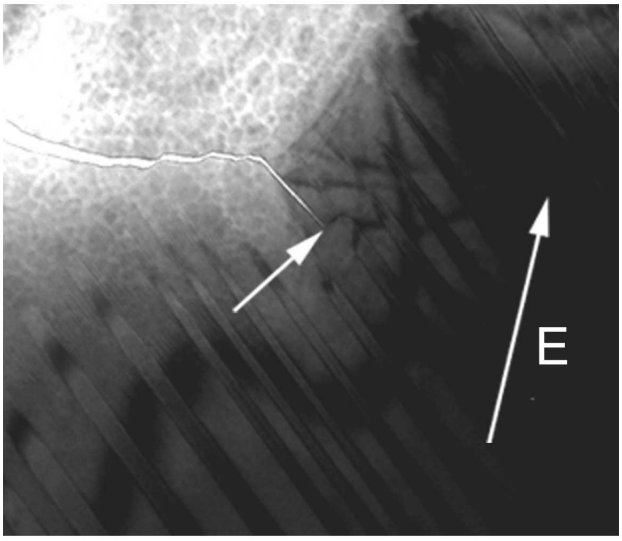

(b)

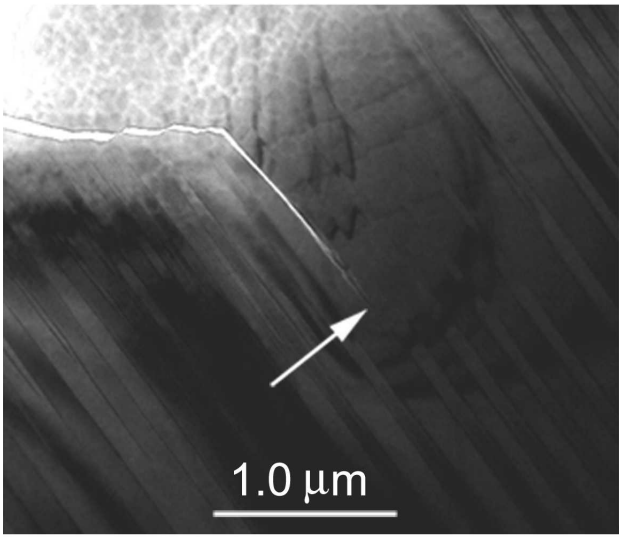

(c)

a direction close to the domain wall. This observation demonstrates that the static electric field, and not just cyclic fields, is capable of inducing fracture in piezoelectric crystals.

The crack growth induced by the static electric field was stable and repeatable. Once the electric field was shut down, the crack growth stopped. When the static field resumed, the crack grew again when the field reached 20 kV/cm. The crack growth was confined to the {101} plane as shown in Fig. 8(c). The repeatability of the critical electric field required to induce crack growth in the two consecutive electric loadings indicates that the field-induced fracture process was not strongly dependent on the domain reconfiguration in the crystal caused by the prior application and subsequent removal of the electric field. The area around the crack tip was examined at higher magnifications and it was confirmed that the crack propagated exactly along the domain wall.

Electric field-induced crack growth was performed in a bulk $0.65Pb(Mg_{1/3}Nb_{2/3})O_3$–$0.35PbTiO_3$ single crystal as well to see if the results obtained from the in situ TEM study are representative. The crystal was cut to dimensions of 6.0 × 3.0 × 0.8 mm with surfaces parallel to the pseudo-cubic {010} planes. Two major surfaces of the crystal (6.0 × 3.0 mm) were polished with 1 μm particle size diamond paste. To minimize residual stresses introduced by grinding and polishing, the crystal was then annealed at 300 °C for 3 h. Au films were evaporated onto the two side surfaces (6.0 × 0.8 mm) as electrodes to provide fields along the ⟨001⟩ direction. The crystal was then loaded mechanically by pressing a Vickers diamond indentor against the {010} surface at 0.5 N for 5 s. The indentor was so oriented that two cracks emitting from the indentation corners would be perpendicular to the field direction while the other two parallel to the field direction, as schematically shown in Fig. 9(a). The Au film electrodes were then connected to a high voltage power supply. Cyclic sinusoidal electric fields of 30 Hz were applied to the crystal along the ⟨001⟩ direction. Optical microscopy with cross-polarized light revealed the electric field-induced growth of the two cracks that were perpendicular to the field. After the initial self-similar extension along the {001} plane, the crack deflected about 45° to follow the {101} domain wall. Figure 9(b) shows the tip of the growing crack under optical microscope after cycling at a nominal field of

FIG. 8. Bright-field TEM images showing the electric field-induced domain wall fracture in a $0.65Pb(Mg_{1/3}Nb_{2/3})O_3$–$0.35PbTiO_3$ single crystal with tetragonal structure: **B**//⟨010⟩; multi-beam condition. (a) The preexisting crack and the regular 90° domain stripes. The in-plane ⟨001⟩ direction is indicated by the bright arrow. The domain wall is parallel to the {101} plane. (b) Crack growth after the first application of a static field of 20 kV/cm. The field was applied along the ⟨001⟩ direction. (c) Crack growth after the second application of the same field.

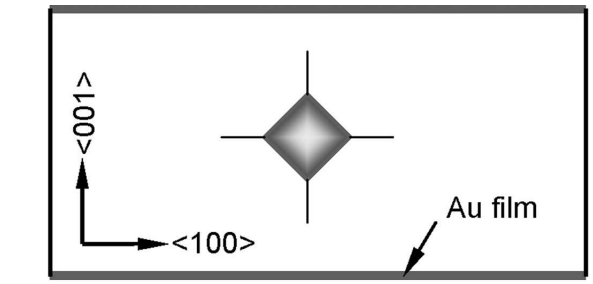

(a)

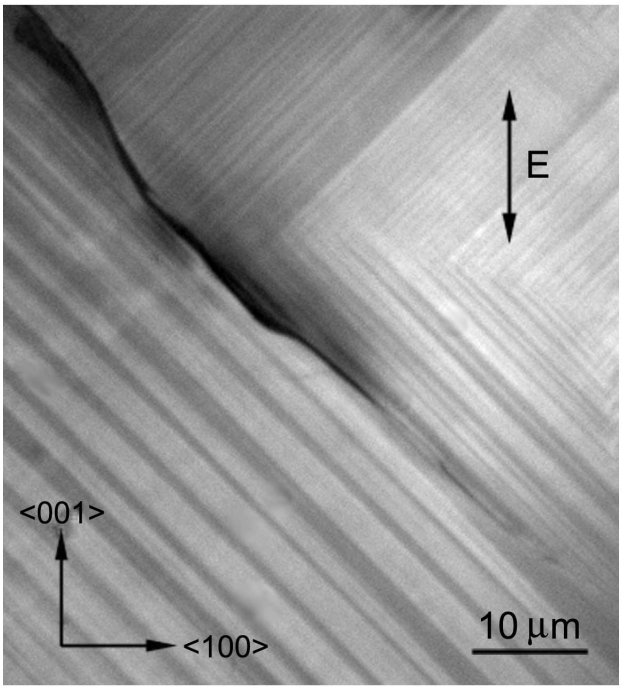

(b)

FIG. 9. Confirmation of the electric field-induced domain wall fracture in a bulk $0.65Pb(Mg_{1/3}Nb_{2/3})O_3$–$0.35PbTiO_3$ single crystal. (a) Specimen geometry of the bulk crystal. The crack was introduced by a Vickers indentation. (b) Optical microscopy image showing the tip of the growing crack after 190,000 cycles at ±4.0 kV/cm. The field was applied along the ⟨001⟩ direction at a frequency of 30 Hz.

±4.0 kV/cm for 190,000 cycles. Therefore, the electric field-induced crack growth behavior in the bulk crystal is the same as that in the thin crystal observed in the TEM.

Although grain boundary is eliminated from single crystals, the domain wall, separating volumes with uniform polarization, is revealed to be a preferred path for electric field-induced fracture. This is due to the incompatible strain at the domain wall. Consider two adjacent 90° domains A and B with the polarization vector parallel to the [001] direction. The applied static electric field is parallel to the polarization of the domain A but perpendicular to the polarization of the adjacent domain B. The piezoelectric strain developed in the domain A without constraints can be expressed as

$$\begin{pmatrix} 0 & 0 & d_{31} \\ 0 & 0 & d_{31} \\ 0 & 0 & d_{33} \\ 0 & d_{15} & 0 \\ d_{15} & 0 & 0 \\ 0 & 0 & 0 \end{pmatrix} \times \begin{pmatrix} 0 \\ 0 \\ E \end{pmatrix} = \begin{pmatrix} d_{31}E \\ d_{31}E \\ d_{33}E \\ 0 \\ 0 \\ 0 \end{pmatrix}, \quad (1)$$

where d_{ij} is the piezoelectric coefficients and E the applied electric field. The piezoelectric strain generated in the domain B without constraints is expressed as

$$\begin{pmatrix} 0 & 0 & d_{31} \\ 0 & 0 & d_{31} \\ 0 & 0 & d_{33} \\ 0 & d_{15} & 0 \\ d_{15} & 0 & 0 \\ 0 & 0 & 0 \end{pmatrix} \times \begin{pmatrix} E \\ 0 \\ 0 \end{pmatrix} = \begin{pmatrix} 0 \\ 0 \\ 0 \\ 0 \\ d_{15}E \\ 0 \end{pmatrix}. \quad (2)$$

Obviously the piezoelectric strains at the domain wall are not compatible to each other and elastic energy will be built up in the close vicinity of the wall. In addition, the 90° domain walls are planar defects and have interfacial energies. Fracture along domain walls would require lower energy than along other crystallographic planes. The domain wall is, therefore, a preferred path for electric field-induced crack growth.

D. Incommensurate phase transformation

Antiferroelectric ceramics have been attracting more attentions due to their potential applications in energy storage devices.[21,22,35] The physics mechanism for the energy storage/release is the antiferroelectric ↔ ferroelectric phase switching controlled by external electric fields. These ceramics are based on the prototypical antiferroelectric $PbZrO_3$ with various dopants such as La, Nb, Sn, and Ti.[21,22,35–40] The dopants serve multiple functions: adjusting the critical field level for the phase switching, enhancing the energy storage volume density, and facilitating ceramic processing. In this section, antiferroelectric polycrystalline ceramics of $Pb_{0.99}Nb_{0.02}[(Zr_{1-x}Sn_x)_{1-y}Ti_y]_{0.98}O_3$ (abbreviated as PZST 100*x*/100*y*/2) were examined with the electric field in situ TEM technique.

In the modified antiferroelectric ceramics, the free energy of the antiferroelectric state and the ferroelectric state is so close that a moderate electric field (<100 kV/cm) could trigger the phase transformation. Figure 10 shows the field-induced transformation in PZST 45/6/2 revealed by polarization measurement. The characteristic double hysteresis loops indicate the antiferroelectric-to-ferroelectric phase transformation at room temperature. The curve with the dashed line was obtained

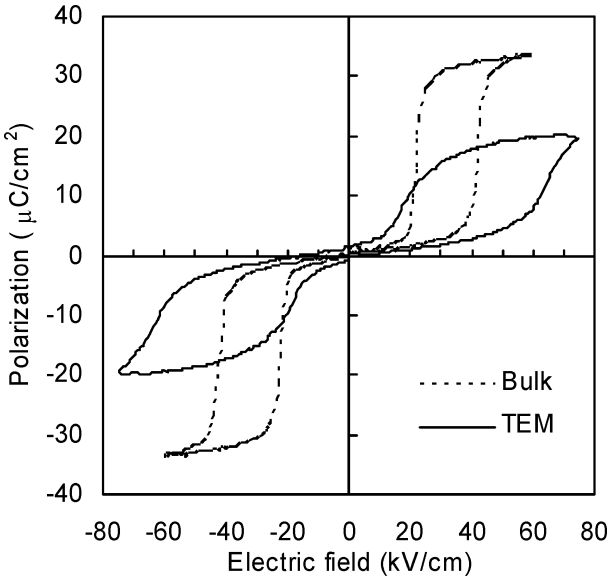

FIG. 10. Electric field-induced antiferroelectric ↔ ferroelectric phase switching characterized by polarization measurement at 4 Hz in the PZST 45/6/2 polycrystalline ceramic. The hysteresis loop with the dashed line was obtained from a standard sample with 12 mm in diameter and 300 μm in thickness. The loop with the solid line was measured from a dimpled TEM specimen electroded in the configuration shown in Fig. 2(a).

from a standard bulk sample with a diameter of 12 mm and a thickness of 300 μm with electric field applied in the thickness direction. The curve with the solid line represents the result from a dimpled TEM specimen with an electrode configuration shown in Fig. 2(a). For the standard bulk sample, the measurement shows a critical field of ~40 kV/cm for the antiferroelectric-to-ferroelectric phase switching and ~20 kV/cm for the backward switching.

As a result of the small difference in the free energy, there is a strong competition between the antiferroelectric ordering and the ferroelectric ordering in the material. The competition leads to the presence of incommensurate modulations.[36–40] The modulation appears as regular fringes along {110} planes in the dark field image and as satellite spots in the selected area electron diffraction pattern. Figure 11 shows the modulations in the PZST 45/6/2 ceramic with a wavelength about 2.1 nm. The satellites can be expressed as $ha^* + kb^* + lc^* \pm \frac{1}{n}\{a^* + b^*\}$, with $n = 7.29$ in Fig. 11(b).

In situ TEM study was carried out on a 3-mm-disk specimen of PZST 45/6/2 polycrystalline ceramic.[19] The evolution of the satellite spots in a ⟨112⟩-zone axis selected area diffraction pattern under static electric fields is shown in Fig. 12. The applied electric field was along the grey line in Fig. 12(b). Initially, the imaged grain displays one set of incommensurate modulations [Fig. 12(a)]. No detectable changes to these satellite spots were observed with applied static electric field up

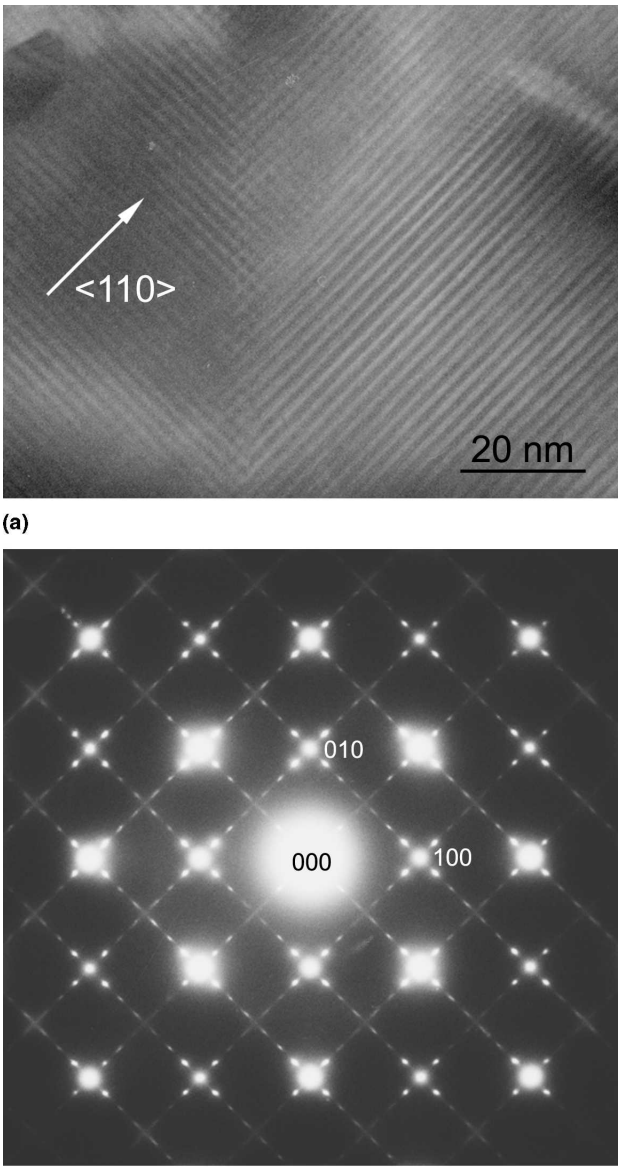

FIG. 11. Incommensurate modulation observed in the PZST 45/6/2 ceramic by TEM. (a) Dark-field image formed with the 110 fundamental spot and its four satellite spots: **B**//<001>; multi-beam condition. The regular fringes with wavelength about 2.1 nm are parallel to the {110} planes. (b) Selected area electron diffraction pattern with zone axis of ⟨001⟩. The diffraction pattern is indexed on the basis of pseudocubic structure.

to 40 kV/cm. At the field level of 48 kV/cm, these satellites become weaker in intensity [Fig. 12(b)]. It should be noted that this field level lies in the close vicinity of the critical field measured from the bulk sample. Careful measurement indicates that the modulation wavelength almost did not change with increasing field strength. When the field strength reached 56 kV/cm, most satellite spots disappeared, as shown in Fig. 12(c). Then the electric field was reduced to 40 kV/cm. Some satellites reappeared, with the strongest ones sitting in the upper-left

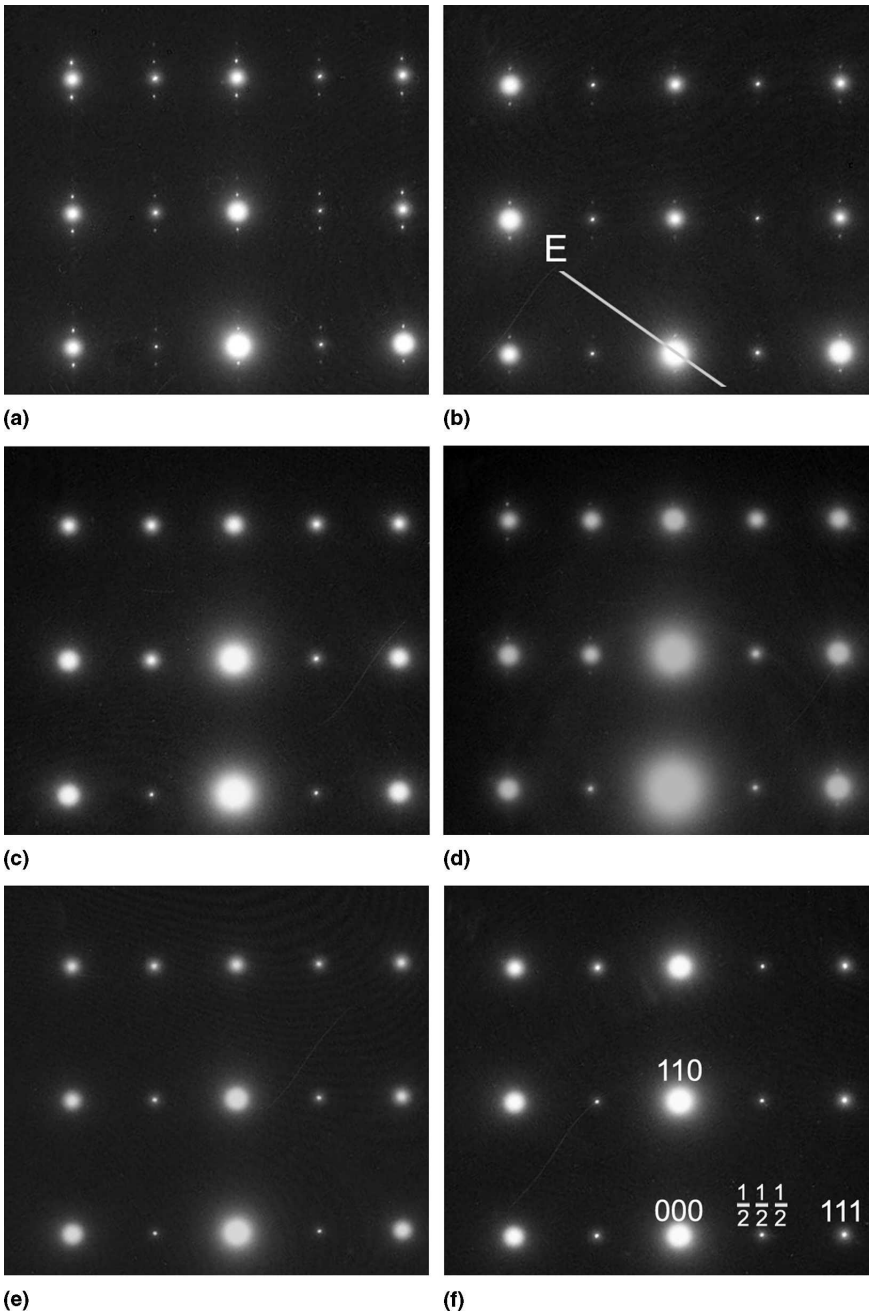

FIG. 12. Evolution of the incommensurate modulation during the electric field-induced antiferroelectric-to-ferroelectric phase transformation in the PZST 45/6/2 ceramic. The field direction is indicated by the gray line in (b). The ⟨112⟩-zone axis selected-area electron diffraction pattern is shown at (a) the initial condition, (b) 48 kV/cm, (c) 56 kV/cm, (d) 40 kV/cm, (e) 56 kV/cm, and (f) 0 kV/cm. The diffraction pattern is indexed on the basis of pseudocubic structure.

and lower-right corners of Fig. 12(d). When the field was raised again to 56 kV/cm [Fig. 12(e)], all the satellite spots completely disappeared. After the electric field was completely removed, no satellite spots were observed to reappear, as shown in Fig. 12(f). This indicates that the induced ferroelectric phase was metastable and the backward phase switching in this grain was sluggish.

In addition to the satellite spots, 1/2{111}-type superlattice reflections were also present in the ⟨112⟩-axis diffraction pattern, as labeled in Fig. 12(f). The structural origin for these superlattice reflections is still under debate.[38–40] However, the present in situ TEM study provides valuable insight into the physics mechanism for the presence of these superlattice spots. It is clear in Fig. 12

that the intensity of the 1/2{111}-type spots does not change with the applied electric field, implying a mechanism that is quite rigid to external disturbance. This seems to be in favor of the oxygen octohedra tilting model.[41]

In situ TEM study was also carried out on a PZST 42/4.5/2 antiferroelectric ceramic. A grain in the electron transparent area happened to have its ⟨001⟩-zone axis parallel to the electron beam. The change of the satellites under external electric fields is shown in Fig. 13. The applied electric field was determined to be along the gray line in Fig. 13(b). Initially, there were two sets of modulations in this grain. The satellite spots were well-defined and in circular shape [Fig. 13(a)]. Upon application of a strong static electric field of 60 kV/cm, one set of the satellites completely disappeared. Most spots of the other set also disappeared, and the remaining satellites are severely distorted with prominent streaking [Fig. 13(b)].

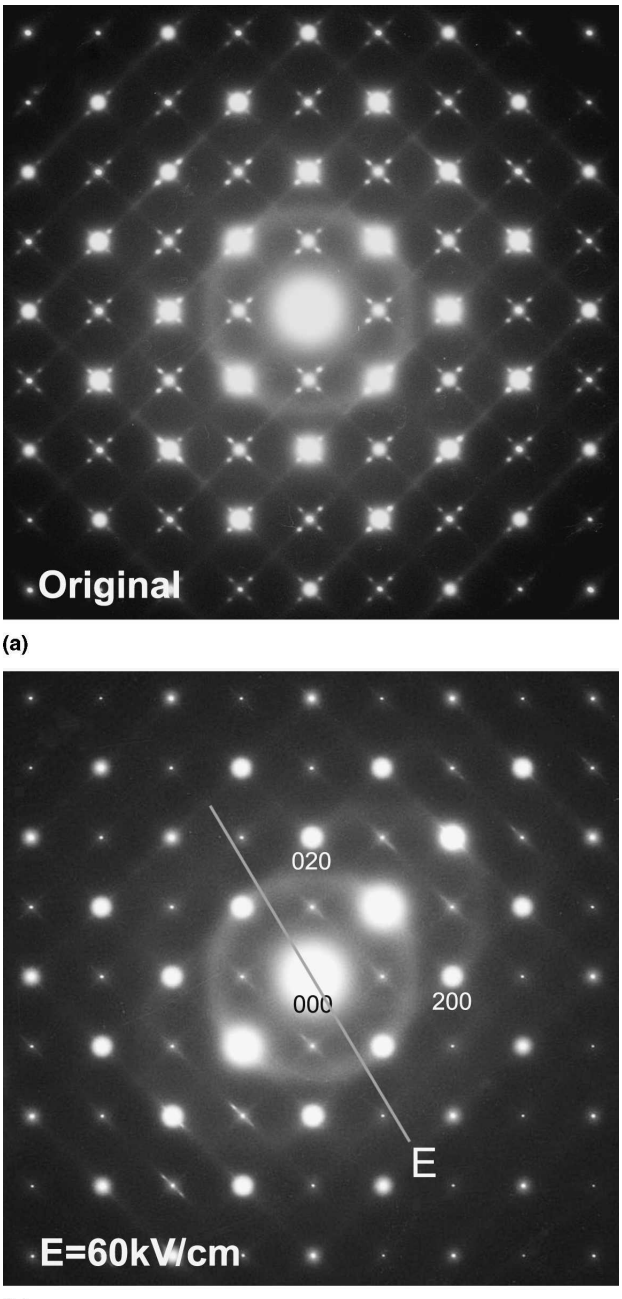

FIG. 13. Change of the satellites in the ⟨001⟩-zone axis diffraction pattern under a strong electric field in the PZST 42/4.5/2 polycrystalline ceramic: (a) initial selected area electron diffraction pattern, and (b) diffraction pattern from the same area at 60 kV/cm. The direction of the applied electric field is indicated by the gray line in (b). The diffraction pattern is indexed on the basis of pseudocubic structure.

The presence of incommensurate modulations in antiferroelectric ceramics is believed to be a result of the competition between the ferroelectric and the antiferroelectric ordering.[39] A continuous increase in the modulation wavelength with increasing temperature was observed previously in ceramics with compositions similar to the PZST 45/6/2 and PZST 42/4.5/2 examined in this study. Such increase was as high as 40% (from 2.1 nm to about 2.94 nm) when the temperature was increased from room temperature to 150 °C.[38] However, our observations on the electric field-induced transformation of the incommensurate modulation did not reproduce the huge change in the wavelength. Instead, the change in wavelength under electric fields was minimal (less than 2%) even at fields close to the critical field for the antiferroelectric-to-ferroelectric transformation. Therefore, the electric field in situ TEM study suggests a different mechanism for the electric field-induced phase transformation from that for the thermally induced one. Further analysis and studies are currently underway and will be reported later.

IV. CONCLUSIONS

Electric field in situ TEM technique is extremely powerful in revealing underlying physics mechanisms of many field-induced phenomena in ferroelectric materials. With the new configuration of electroding on TEM specimens, the following observations were successfully made.

(1) Polarization alignment and domain coalescence were directly observed for nanometer-sized ferroelectric domains.

(2) The electric field-induced grain boundary fracture in ferroelectric polycrystalline ceramics was found to initiate from pores at triple junctions of grain boundaries. A cavition process was involved in both crack initiation and propagation stages. The amorphous phase with high impurities at grain boundaries was melted when ferroelectric ceramics were subjected for extended cycling with bipolar electric fields. The negative pressure originated from the incompatible piezoelectric strain at the grain boundary initiated the cavitation process.

(3) When grain boundary is eliminated in ferroelectric single crystals, 90° domain wall was found to be a preferred path for the electric field-induced fracture. The adjacent domains across the wall have polarization vectors 90° apart. The piezoelectric strains are incompatible at the domain wall when an external field is applied in the direction parallel to one polarization vector. The stored elastic energy may be released by the extension of the crack along the domain wall.

(4) The evolution of incommensurate modulations in antiferroelectric polycrystalline ceramics was also investigated during the electric field-induced antiferroelectric-to-ferroelectric phase transformation. The modulations were found to disappear at a field level close to the critical field for the antiferroelectric-to-ferroelectric transformation. In both PZST 45/6/2 and PZST 42/4.5/2 ceramics, only a small increase (less than 2%) in the wavelength of the modulation was observed prior to the disappearance of the modulation.

ACKNOWLEDGMENTS

This work was partially supported by the National Science Foundation through CAREER Grant No. DMR-0346819. The experimental work was carried out at the Center for Microanalysis of Materials, University of Illinois at Urbana–Champaign and at the Materials & Engineering Physics Program, Ames Laboratory, United States, Department of Energy.

REFERENCES

1. I.A. Blech and E.S. Meieran: Direct transmission electron microscope observation of electrotransport in aluminum thin films. *Appl. Phys. Lett.* **11,** 263 (1967).
2. L. Berenbaum: Electromigration damage of grain-boundary triple points in Al thin films. *J. Appl. Phys.* **42,** 880 (1971).
3. H. Okabayashi, M. Komatsu, and H. Mori: Depth-resolved in-situ TEM observation of electromigration in a submicron-wide layered Al–0.5% Cu line. *Jpn. J. Appl. Phys. Part 1* **35,** 1102 (1996).
4. H. Okabayashi, H. Kitamura, M. Komatsu, and H. Mori: Behavior of electromigration-induced gaps in a layered Al line observed by *in situ* sideview transmission electron microscopy. *Appl. Phys. Lett.* **68,** 1066 (1996).
5. H. Mori, H. Okabayashi, and M. Komatsu: Electromigration in layered Al lines studied by *in-situ* ultra-high voltage electron microscopy. *Thin Solid Films* **300,** 25 (1997).
6. N. Yamamoto, K. Yagi, and G. Honjo: Electron microscopic studies of ferroelectric and ferroelastic $Gd_2(MoO_4)_3$. *Phys. Status Solidi A* **62,** 657 (1980).
7. E. Snoeck, L. Normand, A. Thorel, and C. Roucau: Electron microscopy study of ferroelastic and ferroelectric domain-wall motions induced by the in situ application of an electric field in $BaTiO_3$. *Phase Trans.* **46,** 77 (1994).
8. V. Saikumar, H.M. Chan, and M.P. Hamer: Investigation of ferroelectrics using conventional and in situ electron microscopy, in *Proc. 52nd Annual Meeting of Microscopy Society of America*, edited by G.W. Bailey and A.J. Garratt-Reed (San Francisco Press, San Francisco, CA, 1994), pp. 586–587.
9. X. Lin, C. Murray, and V.P. Dravid: Statics and dynamics of charged interfaces in electroceramics, in *Microscopy and Microanalysis 1998*, edited by G.W. Bailey, K.B. Alexander, W.G. Jerome, M.G. Bond, and J.J. McCarthy. (Springer, New York, 1998), pp. 552–553.
10. A. Krishnan, M.E. Bisher, and M.M.J. Treacy: In situ TEM study of domain propagation in ferroelectric barium titanate and its role in fatigue, in *Ferroelectric Thin Films VII,* edited by R.E. Jones, R.W. Schwartz, S.R. Summerfelt, and I.K. Yoo (Mater. Res. Soc. Symp. Proc. **541,** Warrendale, PA, 1999), p. 475.
11. C.A. Randall, D.J. Barber, and R.W. Whatmore: In situ TEM experiments on perovskite-structured ferroelectric relaxor materials. *J. Microsc.* **145,** 275 (1987).
12. Z.L. Wang and Z.C. Kang: *Functional and Smart Materials: Structural Evolution and Structure Analysis* (Plenum Press, New York, 1998), p. 396.
13. K.D. Johnson and V.P. Dravid: Grain boundary barrier breakdown in niobium donor doped strontium titanate using in situ electron holography. *Appl. Phys. Lett.* **74,** 621 (1999).
14. X. Tan, T. Du, and J.K. Shang: Piezoelectric-actuated in situ transmission electron-microscopy technique for fatigue failure study on constrained metal thin films. *Appl. Phys. Lett.* **80,** 3946 (2002).
15. X. Tan and J.K. Shang: In-situ TEM observations of electric field induced domain switching and microcracking in ferroelectric ceramics. *Mater. Sci. Eng.* **A314,** 157 (2001).
16. Z. Xu, X. Tan, P. Han, and J.K. Shang: In situ TEM study of electric-field-induced microcracking in single crystal $0.66Pb(Mg_{1/3}Nb_{2/3})O_3$–$0.34PbTiO_3$. *Appl. Phys. Lett.* **76,** 3732 (2000).
17. X. Tan, Z. Xu, J.K. Shang, and P. Han: Direct observations of electric field-induced domain boundary cracking in ⟨001⟩ oriented piezoelectric $Pb(Mg_{1/3}Nb_{2/3})O_3$–$PbTiO_3$ single crystal. *Appl. Phys. Lett.* **77,** 1529 (2000).
18. X. Tan and J.K. Shang: In-situ transmission-electron-microscopy study of electric field-induced grain boundary cracking in lead zirconate titanate. *Philos. Mag. A* **82,** 1463 (2002).
19. H. He and X. Tan: In situ transmission-electron-microscopy study of the electric field-induced transformation of incommensurate modulations in a Sn-modified lead zirconate titanate ceramic. *Appl. Phys. Lett.* **85,** 3187 (2004).
20. M.E. Lines and A.M. Glass: *Principles and Applications of Ferroelectrics and Related Materials* (Clarendon Press, Oxford, U.K., 1977).
21. W. Pan, Q. Zhang, A. Bhalla, and L.E. Cross: Field-forced antiferroelectric-to-ferroelectric switching in modified lead zirconate titanate stannate ceramics. *J. Am. Ceram. Soc.* **72,** 571 (1989).
22. P. Yang and D.A. Payne: Thermal stability of field-forced and field-assisted antiferroelectric-ferroelectric phase transformation in $Pb(Zr,Sn,Ti)O_3$. *J. Appl. Phys.* **71,** 1361 (1992).
23. S.E. Park and T.R. Shrout: Ultrahigh strain and piezoelectric behavior in relaxor based ferroelectric single crystals. *J. Appl. Phys.* **82,** 1804 (1997).
24. S. Wada, S. Suzuki, T. Noma, T. Suzuki, M. Osada, M. Kakihana, S.E. Park, L.E. Cross, and T.R. Shrout: Enhanced piezoelectric property of barium titanate single crystals with engineered domain configurations. *Jpn. J. Appl. Phys.* **38,** 5505 (1999).
25. Z.G. Ye: Relaxor ferroelectric complex perovskites: Structure, properties, and phase transitions. *Key Eng. Mater.* **155-156,** 81 (1998).
26. H. Cao and A.G. Evans: Electric-field-induced fatigue crack growth in piezoelectrics. *J. Am. Ceram. Soc.* **77,** 1783 (1994).
27. J.K. Shang and X. Tan: A maximum strain criterion for electric-field-induced fatigue-crack propagation in ferroelectric ceramics. *Mater. Sci. Eng.* **A301,** 131 (2001).

28. G.S. White, A.S. Raynes, M.D. Vaudin, and S.W. Freiman: Fracture behavior of cyclically loaded PZT. *J. Am. Ceram. Soc.* **77,** 2603 (1994).
29. C.S. Lynch, W. Yang, L. Collier, Z. Suo, and R.M. McMeeking: Electric field induced cracking in ferroelectric ceramics. *Ferroelectrics* **166,** 11 (1995).
30. R.M. McMeeking: Electrostrictive stresses near crack-like flaw. *J. Appl. Math. Phys.* **40,** 615 (1989). ZAMP.
31. Z. Suo: Mechanics concepts for failure in ferroelectric ceramics, in *Smart Structures and Materials*, edited by G.K. Haritos and A.V. Srinivasan (ASME, New York, 1991), AD Vol. 24/AMD Vol. 123, p.1.
32. E.K. Beauchamp: Effect of microstructure on pulse electric strength of MgO. *J. Am. Ceram. Soc.* **54,** 484 (1971).
33. H.C. Ling and D.D. Chang: In situ observation of electrode melting in multilayer ceramic capacitors. *J. Mater. Sci.* **24,** 4128 (1989).
34. H. Kanai, O. Furukawa, S. Nakamura, and Y. Yamashita: Effect of stoichiometry on the dielectric properties and life performance of $(Pb_{0.875}Ba_{0.125})[(Mg_{1/3}Nb_{2/3})_{0.5}(Zn_{1/3}Nb_{2/3})_{0.3}Ti_{0.2}]O_3$ relaxor dielectric ceramic: Part II, life performance. *J. Am. Ceram. Soc.* **76,** 459 (1993).
35. C.K. Campbell, J.D. van Wyk, and R. Chen: Experimental and theoretical characterization of an antiferroelectric ceramic capacitor for power electronics. *IEEE Trans. Comp. Pack. Technol.* **25,** 211 (2002).
36. Y. Chang, J. Lian, and Y. Wang: One-dimensional regular arrays of antiphase domain boundaries in antiferroelectric tin-substituted lead zirconate titanate ceramics. *Appl. Phys. A* **36,** 221 (1985).
37. J.S. Speck, M. De Graef, A.P. Wilkinson, A.K. Cheetham, and D.R. Clarke: Hierarchical domain structures and in situ domain migration in the antiferroelectric ceramic PLSnZT. *J. Appl. Phys.* **73,** 7261 (1993).
38. Z. Xu, D. Viehland, and D.A. Payne: An incommensurate-commensurate phase transformation in antiferroelectric tin-modified lead zirconate titanate. *J. Mater. Res.* **10,** 453 (1995).
39. D. Viehland, X.H. Dai, J.F. Li, and Z. Xu: Effects of quenched disorder on La-modified lead zirconate titanate: Long- and short-range ordered structurally incommensurate phases, and glassy polar clusters. *J. Appl. Phys.* **84,** 458 (1998).
40. J. Knudsen, D.I. Woodward, and I. Reaney: Domain variance and superstructure across the antiferroelectric/ferroelectric phase boundary in $Pb_{1-1.5x}La_x(Zr_{0.9}Ti_{0.1})O_3$. *J. Mater. Res.* **18,** 262 (2003).
41. D. Viehland, Z. Xu, and D.A. Payne: Origin of F spots and stress sensitivity in lanthanum lead zirconate titanate. *J. Appl. Phys.* **74,** 7454 (1993).